

Full Length Article

Four nanoscale-extended equations of state: Phase behaviour of confined fluids in shale reservoirs

Kaiqiang Zhang^a, Paitoon Tontiwachwuthikul^b, Na Jia^{a,*}, Songyan Li^c^a Petroleum Systems Engineering, Faculty of Engineering and Applied Science, University of Regina, Regina, Saskatchewan S4S 0A2, Canada^b Clean Energy Technologies Research Institute (CETRI), Faculty of Engineering and Applied Science, University of Regina, Regina, Saskatchewan S4S 0A2, Canada^c College of Petroleum Engineering, China University of Petroleum (East China), Qingdao 266580, China

ARTICLE INFO

Keywords:

Confined fluids

Phase behaviour

Shale reservoirs

Nanoscale-extended equations of state

Intermolecular interactions

ABSTRACT

In this paper, the thermodynamic phase behaviour of pure and mixing nanoconfined fluids in shale reservoirs are studied. First, an analytical generalized equation of state (EOS) is developed by including the effects of pore radius and intermolecular interactions. Based on the generalized EOS, four extended cubic EOS are proposed and used to calculate the thermodynamic phase behaviour. The four extended cubic EOSs, the extended van der Waals (vdW), Redlich – Kwong (RK), Soave – Redlich – Kwong (SRK), and Peng – Robinson (PR) EOSs, are found to accurately predict the pressure–volume (P–V) diagrams of different systems in nanopores. More specifically, the extended RK (E-RK) EOS may fail to accurately calculate the phase behaviour at high temperatures and the extended PR (E-PR) EOS is more accurate for liquid phase pressure calculations. The overall calculated P–V diagrams for the pure components in nanopores from the extended EOS shift up and right relative to those of the bulk-phase case and the EOS only including the intermolecular interactions. Furthermore, as a physical meaningless phenomenon, the negative pressure state is completely avoided in the calculated P–V diagrams from the extended EOSs. Compared to the measured bubble-point pressure (P_b) for the four different confined mixing fluids, the E-vdW, E-RK, and E-SRK EOS provide accurate estimates of P_b with overall percentage average absolute deviations (AAD%) of 10.95%, 12.07%, and 9.37%, respectively. The proposed extended EOSs are capable to accurately predict the critical properties and their shifts in nanopores. A bottom limit for the continuous reduction of the critical properties by decreasing the pore radius is obtained from the proposed extended EOSs, which is, for example, 5 nm for C_8H_{18} .

1. Introduction

Recently, concerns about nanoconfined fluids have emerged because of their wide range of applications, such as energy storage [1], heterogeneous catalysis [2], separation process [3], and oil/gas fluids in tight and shale formations [4,5]. It is well known that at the nanometer scale, the confinement effect is so strong that the fluid behaviour changes substantially even in qualitative observations [6]. For example, slight energy dissipation caused by friction in the confined fluids can induce a series detectable changes, while these types of changes cannot be noticed in the bulk phase [7,8]. Presently, few laboratory experiments, even though at the lab scale [9], are available in the public domain to study confined fluids at the nanometer scale due to the extremely high measurement precision and enlargement requirements of observation and/or imaging systems [10], as well as the associated costs [11]. Most previous studies on confined fluids at the nanometer scale were mainly conducted through theoretical methods,

including the use of equations of state (EOSs) [12,13], molecular simulations [14,15], density functional theory [16,17], and Kelvin equation [18,19]. The last three theoretical methods are inefficient in calculations due to the heavily-loaded mathematical formulations and complex computational frameworks. Thus, the cubic EOS is a practical alternative approach for evaluating the nanoconfined phase behavior.

The phase behaviour of the confined fluids is of great importance in different scientific and industrial fields. In particular, phase diagrams, bubble-point pressures, and critical properties of confined fluids are key factors for system characterizations [20–23]. For example, in the oil and gas industry, tight and shale fluids in an extremely confined formation is a typical case of a confined fluid at the nanometer scale, where the fluid undergoes substantial phase changes attributed to the shifts of the critical properties [24,25]. A previous literature showed that the bubble point pressure of a Bakken oil- CO_2 system significantly decreased, while the upper dew-point pressure increased and lower dew-point pressure decreased with an increasing confinement effect

* Corresponding author.

E-mail address: Na.Jia@Uregina.ca (N. Jia).<https://doi.org/10.1016/j.fuel.2019.03.095>

Received 2 February 2019; Received in revised form 13 March 2019; Accepted 17 March 2019

Available online 04 April 2019

0016-2361/ © 2019 Elsevier Ltd. All rights reserved.

[26]. In addition, the locus of the critical properties demonstrates that the boundaries of the phase change for mixtures, which is one of the bases for binary phase diagrams [27]. Moreover, the critical properties are commonly used to calculate the pressure–volume–temperature (PVT) and thermodynamic properties based on the corresponding state principle. In the literature, the critical properties of some confined pure substances were found to shift with pore radius reductions, which were roughly predicted using some empirical correlations [28,29]. The above-mentioned fluid phase behaviour studies at the nanometer scale were all based on the existing EOSs that include only the effect of the pore radius or intermolecular interactions. Thus far, no work has been presented where the phase properties of the pure and mixing confined fluids at the nanometer scale were calculated analytically by concurrently including the effects of pore radius, molecule–molecule (m–m), and molecule–wall (m–w) interactions.

In this study, an analytical generalized EOS, which includes the combined effects of pore radius, m–m interactions, and m–w interactions, is developed to calculate the phase properties of pure and mixing confined fluids at nanometer scale. On a basis of the generalized EOS, four extended cubic EOS, the extended van der Waals (E-vdW), Redlich–Kwong (E-RK), Soave–Redlich–Kwong (E-SRK), and Peng–Robinson (E-PR) EOS, are proposed and used to calculate the fluid phase behaviour under the confinement effect. The phase diagrams, bubble-point pressures, and critical properties of single components, such as CO₂, CH₄, and C₈H₁₈, and mixtures, such as C₁₀H₂₂–CH₄, N₂–n-C₄H₁₀, and C₈H₁₈–CH₄, are determined from the four extended cubic EOSs at different temperatures and pore radii, which are compared to and verified by the measured results at the same conditions.

2. Experimental

In this study, N₂, CO₂, and alkanes of C₁–C₁₀ are applied, whose critical temperature, pressure, and volume, constants of the vdW EOS, as well as the Lennard–Jones and square-well potential parameters are summarized [30–33] in Table 1. The pressure–volume–temperature (PVT) tests for the n-C₄H₁₀–N₂ mixture was conducted at temperatures of *T* = 299.15 and 324.15 K by applying a PVT apparatus connected to a shale sample [34]. It is worthwhile to mention that the shale sample was oil-wetting and the pore radius was around 5 nm. In the experiments, the purities of the used n-C₄H₁₀ and N₂ equal to 99.998% and 99.99%, respectively. In addition, the PVT tests of the C₈H₁₈–CH₄ and

C₁₀H₂₂–CH₄ mixtures were conducted at *T* = 311.15 and 325.15 K in silica-based mesoporous materials, SBA-15 and SBA-16, whose pore radii are *r_p* = 3.5 and 3.7 nm [35]. Table 1 summarizes the measured bubble point pressures of the mixtures aforementioned. The detailed experimental information can be found in the previous studies [34,35]. In brief, the pore sizes for the shale samples were characterized from the scanning electron microscopy coupled with the energy-dispersive X-ray spectroscopy, while those for the silica-based mesoporous media were analyzed from the transmission electron microscopy.

3. Theory

3.1. Derivations of the generalized EOS

A generalized EOS for calculating the nanoconfined fluid is developed, which includes the confinement-induced effects and intermolecular interactions. The schematic diagram of the nanopore network model, including the pore shape, and configuration energy are shown in Fig. S1. In addition, new thermodynamic formulations based on four classical cubic EOSs, the vdW, RK, SRK, and PR EOS, are developed and applied for the nanoconfined phase behavior calculations. The specific mathematical formulation of the generalized EOS is shown as,

$$P(N, V, T) = \frac{nRT}{V - nb} - \frac{n^2C}{V^2} \left[a - 2\varepsilon_{LJ}\sigma_{LJ}^3 \left(\frac{c_1}{\sqrt{A}} + \frac{c_2}{A} \right) \right] + (nN_A \cdot \varepsilon_{sw}) \left(\frac{nb\theta}{V^2} \right) \left(1 - \frac{nb}{V} \right)^{\theta-1} (1 - F_{pr}) (1 - e^{-N_A \varepsilon_{sw}/RT}) \quad (1)$$

where *V* is the total volume, *R* is the universal gas constant, *T* is the temperature, *a* and *b* are the volume parameters of the cubic EOS, *N_A* is the Avogadro constant, *ε_{LJ}* is the molecule–molecule Lennard–Jones energy parameter, *σ_{LJ}* is the molecule–molecule Lennard–Jones size parameter, *F_{pr}* is the fraction of the randomly distributed fluid molecules in the square-well region of the pores, *c₀*, *c₁* and *c₂* are the numeric coefficients, and *θ* is a geometric term. Basically, the molecule–molecule interactions based on the Lennard–Jones potential and the molecule–wall interactions from the square-well potential are concurrently considered in the EOS for the first time, which are presented in the second and last term right-hand side, respectively. The detailed derivations for the generalized EOS are stated in the Supporting Information.

Table 1

Measured [34,35] and calculated bubble-point pressures for the C₁₀H₂₂–CH₄, and C₈H₁₈–CH₄ and N₂–n-C₄H₁₀ mixtures at different temperatures and pore radii.

System (mol.%)	<i>T</i> (K)	<i>r_p</i> (m)	<i>P_{b-BP}</i> ^a (kPa)	<i>P_b</i> ^b (kPa)	Change ^c (%)	<i>P_{b-EvdW}</i> ^d (kPa)	AD (%)	<i>P_{b-ERK}</i> ^e (kPa)	AD (%)	<i>P_{b-ESRK}</i> ^f (kPa)	AD (%)	<i>P_{b-EPR}</i> ^g (kPa)	AD (%)
5.40 N ₂ –94.60 C ₄	299.15	5.0 × 10 ^{−9}	3390.6	4268.5	25.89	3967.1	7.06	3684.3	13.69	3907.1	8.47	4230.1	0.90
	324.15		3429.5	4105.8	19.72	4017.1	2.16	3767.4	8.24	4142.9	0.90	4552.6	10.88
	299.15	3.5 × 10 ^{−9}	3115.1	4035.5	29.55	3823.7	5.25	3435.7	14.86	3987.0	1.20	4435.7	9.92
	324.15		3189.6	3883.8	21.76	3915.7	8.21	3596.3	7.40	3903.2	0.50	4469.6	15.08
90.00 C ₁₀ –10.00 C ₁	311.15	3.5 × 10 ^{−9}	2579.0	1669.0	35.28	1988.9	19.17	1874.3	12.30	2054.9	23.12	2631.4	57.66
		3.7 × 10 ^{−9}	2579.0	2034.0	21.13	1856.3	8.74	1802.9	11.36	1978.6	2.72	2687.8	32.14
	325.15		2717.0	2220.0	18.29	2642.3	19.02	2411.2	8.61	2819.4	27.00	2941.7	32.51
90.00 C ₈ –10.00 C ₁	311.15	3.5 × 10 ^{−9}	2579.0	2468.0	9.16	2099.5	14.93	1987.6	19.47	2236.7	9.37	2816.1	14.10
		3.7 × 10 ^{−9}	2503.0	1765.0	29.48	1901.7	7.74	1767.2	0.21	1923.3	8.97	2727.3	54.52
			2503.0	2186.0	12.66	1810.4	17.18	1646.7	24.67	1935.5	11.46	2540.2	16.20
AAD (%)			–	–	–	–	10.95	–	12.07	–	9.37	–	24.39
MAD (%)			–	–	–	–	19.17	–	24.67	–	27.00	–	57.70

Notes:

^a Measured bubble-point pressure in bulk phase.

^b Measured bubble-point pressure at the pore radius of *r_p*.

^c Change of the measured bubble-point pressure in bulk phase and porous medium in percentage.

^d Calculated bubble-point pressure at *r_p* from the extended van der Waals equation of state.

^e Calculated bubble-point pressure at *r_p* from the extended Redlich–Kwong equation of state.

^f Calculated bubble-point pressure at *r_p* from the extended Soave–Redlich–Kwong equation of state.

^g Calculated bubble-point pressure at *r_p* from the extended Peng–Robinson equation of state.

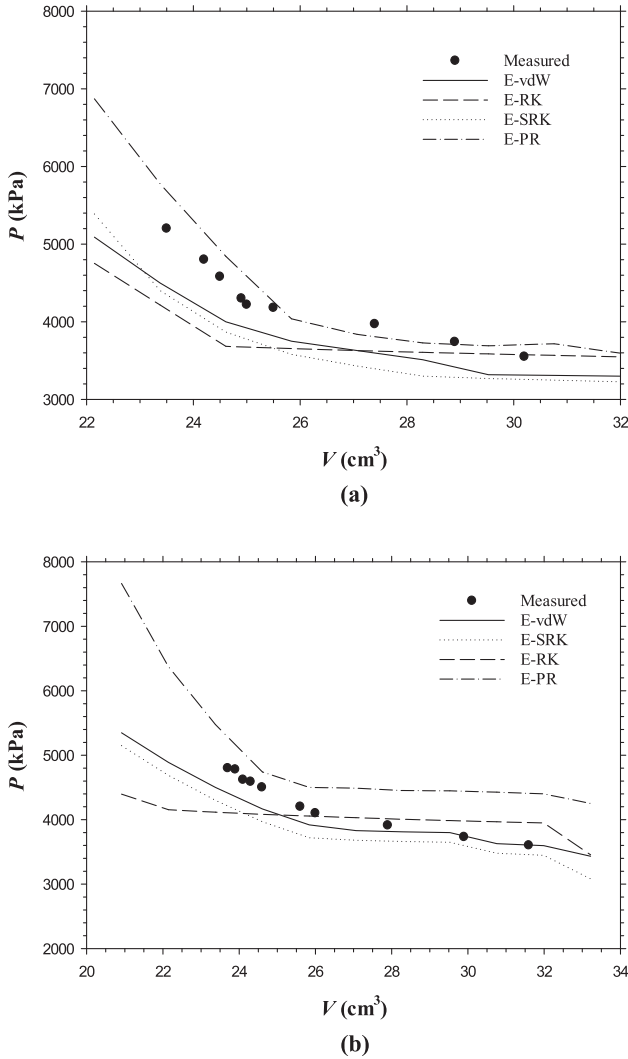


Fig. 1. Measured [34] and calculated pressure–volume isotherms for the 5.40 mol.% N_2 –94.60 mol.% n - C_4H_{10} mixtures from the extended vdW, RK, SRK, and PR equations of state at $r_p = 5.0$ nm and the temperatures of (a) $T = 299.15$ K and (b) $T = 324.15$ K.

3.2. Extensions of the generalized EOS

The generalized EOS can be reformulated to be different specific cubic EOSs by adopting different mixing rules for the function C . More specifically, Eq. (1) is the vdW EOS if the function C is independent of the temperature and density. Moreover, the function C can be considered to be dependent on the temperature and density as follows [36],

$$C = \frac{V^2}{\sqrt{T}} \ln\left(\frac{V}{V + nb}\right) \quad (2a)$$

$$C = (\sqrt{T})^{-i} V^2 \cdot \ln\left(\frac{V}{V + nb}\right) \quad (2b)$$

$$C = (\sqrt{T})^{-i} V^2 \cdot \ln\left(\frac{V - nb}{V + nb}\right) \quad (2c)$$

where i is constant. Three different EOS are derived by substituting Eqs. 2(a–c) into Eq. (1),

$$P(N, V, T) = \frac{nRT}{V - nb} - \frac{n^2}{\sqrt{T}V(V + nb)} \left[a - 2\varepsilon_{LJ}\sigma_{LJ}^3 \left(\frac{c_1}{\sqrt{A}} + \frac{c_2}{A} \right) \right] + (nN_A \cdot \varepsilon_{sw}) \left(\frac{nb\theta}{V^2} \right) \left(1 - \frac{nb}{V} \right)^{\theta-1} (1 - F_{pr}) (1 - e^{-N_A \varepsilon_{sw}/RT}) \quad (3a)$$

$$P(N, V, T) = \frac{nRT}{V - nb} - \frac{n^2(\sqrt{T})^{-i}}{V(V + nb)} \left[a - 2\varepsilon_{LJ}\sigma_{LJ}^3 \left(\frac{c_1}{\sqrt{A}} + \frac{c_2}{A} \right) \right] + (nN_A \cdot \varepsilon_{sw}) \left(\frac{nb\theta}{V^2} \right) \left(1 - \frac{nb}{V} \right)^{\theta-1} (1 - F_{pr}) (1 - e^{-N_A \varepsilon_{sw}/RT}) \quad (3b)$$

$$P(N, V, T) = \frac{nRT}{V - nb} - \frac{n^2(\sqrt{T})^{-i}}{(V - nb)(V + nb)} \left[a - 2\varepsilon_{LJ}\sigma_{LJ}^3 \left(\frac{c_1}{\sqrt{A}} + \frac{c_2}{A} \right) \right] + (nN_A \cdot \varepsilon_{sw}) \left(\frac{nb\theta}{V^2} \right) \left(1 - \frac{nb}{V} \right)^{\theta-1} (1 - F_{pr}) (1 - e^{-N_A \varepsilon_{sw}/RT}) \quad (3c)$$

In summary, Eqs. (1) and 3(a–c) are the newly-derived thermodynamic formulations of the vdW, RK, SRK, and PR EOSs for confined fluids in nanopores.

3.3. Critical property calculations

Generally, the critical properties in the EOS are calculated under the following two classic conditions [30],

$$\left(\frac{\partial P}{\partial V} \right)_{T=T_c} = 0 \quad (4a)$$

$$\left(\frac{\partial^2 P}{\partial V^2} \right)_{T=T_c} = 0 \quad (4b)$$

Due to the complexity of the pressure terms in Eqs. (1) and 3(a–c), Eqs. (4a) and b are numerically calculated using a modified Newton-Raphson scheme, which is applied for two-unknown iterations, with different initial estimates of the critical pressure and temperature for the confined fluids in nanopores. The analytical solutions of Eqs. (4a) and b as well as the other required elements of the Jacobian matrix, $\frac{\partial^2 P}{\partial V \partial T}$, $\frac{\partial^3 P}{\partial V^2 \partial T}$, are pre-requisite. It should be noted that the parameters of a , b , σ_{LJ} , ε_{LJ} , ε_{sw} , δ_{sw} , and r_p are given, wherein tabulated values of a and b in each EOS are used and δ_{sw} is specified to be equal to σ_{LJ} in this study. It is worthwhile to mention that the constant b for each EOS is assumed to be equivalent to the vdW-EOS constant. The shifts of the critical properties in nanopores can be directly calculated. In addition, the critical temperature and pressure and shifts of the critical properties of a mixture can be calculated by applying a simple mixing rule [30],

$$T_c = \sum x_i T_{ci}, \quad P_c = \sum x_i P_{ci} \quad (5)$$

4. Results and discussion

4.1. Phase diagram

The P–V diagrams of the N_2 (5.40 mol.%)– n - C_4H_{10} (94.60 mol.%) mixtures at the temperatures of $T = 299.15$ and 324.15 K and pore radius of $r_p = 5.0$ nm are calculated from the extended vdW, RK, SRK, and PR EOS in Eqs. (1) and 3(a–c). The calculated data are compared with the measured results [34] and plotted in Fig. 1a and b. Similar to the N_2 – n - C_4H_{10} P–V diagram in the bulk phase, the measured and calculated pressures are all reduced when the volume increases in two distinct ranges. The pressure is rapidly decreased in the first high pressure range while the pressure reduction with respect to the volume increase becomes much more gradual in the second low pressure range. The corresponding ordinate value of the intersection point of the first and second ranges intersect is the bubble-point pressure. The calculated P–V diagrams are found to be slightly different from the measured data at different conditions. More precisely, the calculated pressures from the E-PR EOS are moderately higher while those from the other three extended EOSs are lower than the measured pressure at the same volume. It is inferred that the universal constant b used in each extended EOS and some empirical

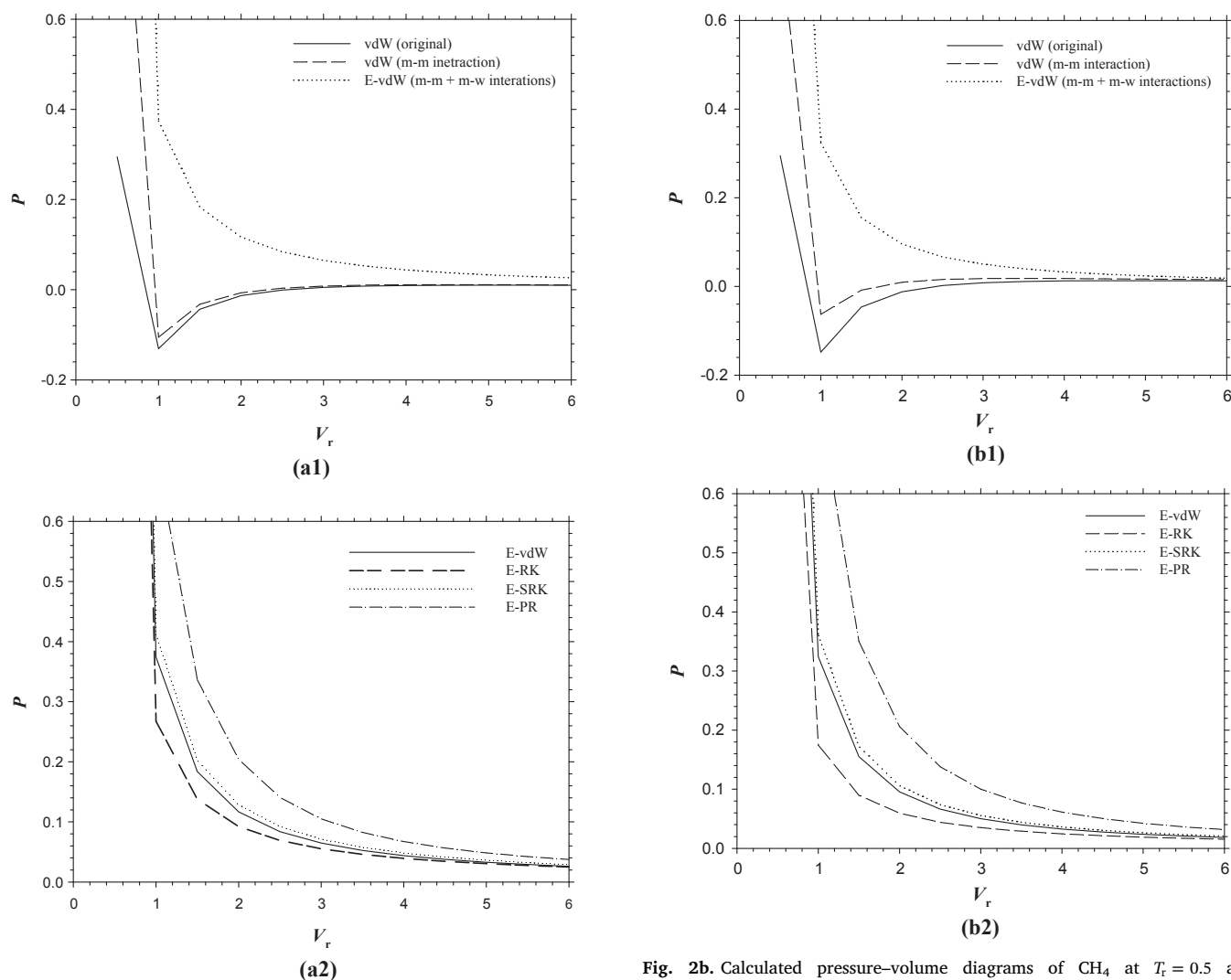


Fig. 2a. Calculated pressure–volume diagrams of CO_2 at $T_r = 0.5$ and $V_r = 0.5 - 6.0$ (a1) in the bulk phase from the original vdW EOS, at the pore radius of 1 nm from the vdW EOS including only the molecule–molecule interaction and the extended vdW EOS including the molecule–molecule and molecule–wall interactions; (a2) at the pore radius of 1 nm from the extended vdW, RK, SRK, and PR EOSs.

values (e.g., ρ_{\max} , $f(A)$, or LJ/SW potential parameters) used in the model may cause deviations. The measured data were also affected by the fluid sorption, which may have changed the composition to some extent, and thus, the equilibrium phase behaviour become different. It should be noted that the E-SRK and E-PR EOS perform better at a higher temperature of $T = 324.15$ K, which is attributed to the addition of the temperature-dependent function C in these two extended EOS. Overall, the extended vdW, SRK, and PR EOSs are capable of predicting the general trends and specific values of the P–V diagrams at the nanometer scale, whereas the E-RK EOS may fail to predict the pressures, especially at high temperatures.

In Figs. 2a–c, the calculated P–V diagrams for CO_2 , CH_4 , and C_8H_{18} in the bulk and nanoconfined cases from the original vdW EOS, vdW EOS including only m–m interactions, and the four extended EOS including both m–m and m–w interactions at the reduced temperature (T_r) of $T_r = 0.5$ and volumes (V_r) of $V_r = 0.5 - 6.0$ are presented. It is seen from the figures that the pressure is decreased with increasing volume. More specifically, Fig. 2a1 clearly indicates that the results from either the vdW EOS including only the m–m or the E-vdW EOS including both the m–m and m–w interactions in nanopores shift upward compared to the curve of the bulk case, which is resulted from the enhanced confinement

Fig. 2b. Calculated pressure–volume diagrams of CH_4 at $T_r = 0.5$ and $V_r = 0.5 - 6.0$ (b1) in the bulk phase from the original vdW EOS, at the pore radius of 1 nm from the vdW EOS including only the molecule–molecule interaction and the extended vdW EOS including the molecule–molecule and molecule–wall interactions; (b2) at the pore radius of 1 nm from the extended vdW, RK, SRK, and PR EOSs.

effect in nanopores. The calculated pressure from the E-vdW EOS is even higher than the vdW EOS including only the m–m interactions. This is mainly attributed to the addition of the short-range intermolecular force between the molecules and wall [37,38]. In Fig. 2a2, the calculated CO_2 pressures at $r_p = 1$ nm, $T_r = 0.5$, and $V_r = 0.5 - 6.0$ from the E-vdW, E-RK, E-SRK, and E-PR are plotted versus the reduced volumes. The calculated pressures from the E-PR and E-SRK EOS are higher while those from the E-RK EOS are lower compared to the results from the E-vdW EOS. The deviations of the different calculated pressures in Figs. 2a1 and a2 become smaller with the increasing reduced volume.

In Figs. 2b1 and b2, the P–V diagrams of CH_4 share a similar overall pattern with those of the CO_2 case. Two main differences occur in the P–V diagrams of C_8H_{18} , which are inconsistent with the overall patterns of the CO_2 and CH_4 cases, shown in Fig. 2c1 and c2 and described as follows: First, there are more negative values of the calculated pressures from the original vdW EOS in bulk phase and from the vdW EOS including only m–m interaction in the nanopores. The negative pressures are present for CO_2 , CH_4 , and C_8H_{18} in the bulk phase and nanopores with only m–m interactions. For gases, the negative pressure state is generally considered to be physically meaningless [30]. This is because the theoretical basis of the negative pressure state, which is an infinite volume corresponds to an approaching-zero pressure from the

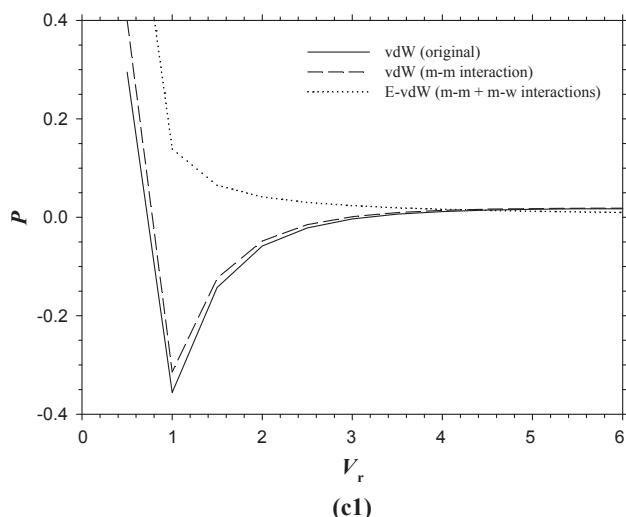


Fig. 2c. Calculated pressure–volume diagrams of C_8H_{18} at $T_r = 0.5$ and $V_r = 0.5 - 6.0$ (c1) in the bulk phase from the original vdW EOS, at $r_p = 1$ nm from the vdW EOS including only the molecule–molecule interaction and the extended vdW EOS including the molecule–molecule and molecule–wall interactions; (c2) at $r_p = 1$ nm from the extended vdW, RK, SRK, and PR EOSs.

ideal gas EOS, is obviously not true. This problem is completely avoided by adding the m–w interactions into the EOS model, and no negative pressures are found for the gas cases in Figs. 2b1 and b1. On the other hand, the negative pressure state is valid for liquids when they are stretched or under tension [39]. The negative pressure state for liquids is always considered to be a metastable state, which is also effectively modified by means of the extended EOS. Second, there are smaller deviations of the calculated pressures from the four extended EOS, especially a better result from the E-PR EOS. Thus, it is concluded that the E-PR EOS is more accurate for the liquid pressure calculations.

The newly-developed four extended EOSs are subsequently applied to calculate the P–V diagrams for the 90.00 mol.% C_8H_{18} –10.00 mol.% CH_4 and 90.00 mol.% $C_{10}H_{22}$ –10.00 mol.% CH_4 mixtures at $T = 311.15$ and 325.15 K and $r_p = 3.5$ and 3.7 nm, which are compared to the measured data [35] and plotted in Fig. 3a–c. Overall, the measured pressures are always slightly higher than the calculated pressures from the E-vdW, E-RK, and E-SRK EOSs but moderately lower than those from the E-PR EOS. It should be noted from the literature [29] and the above-mentioned findings that the pressures should be reduced as the pore radius increases with constant volume. However, the measured pressures are substantially increased when the pore radius is increased from 3.5 to 3.7 nm in Figs. 3a1

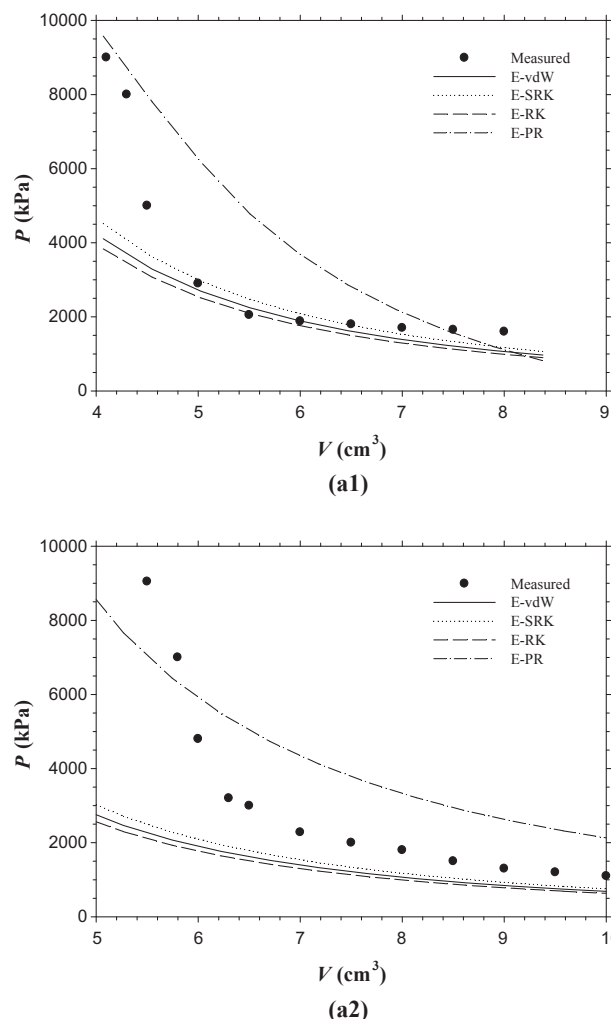


Fig. 3a. Measured [35] and calculated pressure–volume isotherms from the extended vdW, RK, SRK, and PR EOSs for the 90.00 mol.% $C_{10}H_{22}$ –10.00 mol.% CH_4 mixtures at $T = 311.15$ K and (a1) $r_p = 3.5$ nm and (a2) $r_p = 3.7$ nm.

and a2. It is clearly that the calculated pressures from the four extended EOSs are considerably decreased as the pore radius increases. The temperature effect on the P–V diagrams can be studied by comparing Figs. 3a and 3b, since these two figures show the P–V diagrams of the 90.00 mol.% $C_{10}H_{22}$ –10.00 mol.% CH_4 system at the same conditions but different temperatures of $T = 311.15$ and 325.15 K. It is found from the figures that the calculated pressures are affected by the temperature to a small extent and slightly increase at a higher temperature. Fig. 3c shows the P–V diagrams of the 90.00 mol.% C_8H_{18} –10.00 mol.% CH_4 mixtures at the exact same conditions of Fig. 3a. Although the properties of $C_{10}H_{22}$ and C_8H_{18} are found to have a marginal difference, the P–V diagrams of the two different systems are significantly different, even at the same temperature and pore radius. Thus, it is concluded that, compared to the temperature, the compositions affect the phase behaviour to a larger extent in the nanopores.

4.2. Bubble-point pressure

The bubble-point pressure (P_b), as aforementioned, is determined by intersecting the first and second ranges of the P–V diagram [30], whose corresponding ordinate value is determined to be the bubble-point pressure. On a basis of the P–V diagrams in Figs. 3–5, the P_b for the $C_{10}H_{22}$ – CH_4 , C_8H_{18} – CH_4 and N_2 – n - C_4H_{10} mixtures are calculated from the E-vdW, E-RK, E-SRK, and E-PR EOS in the nanopores, which are compared with the measured P_b in the bulk phase and nanopores and are listed in Table 1. More precisely, the measured bubble-point pressures of the N_2 – n - C_4H_{10}

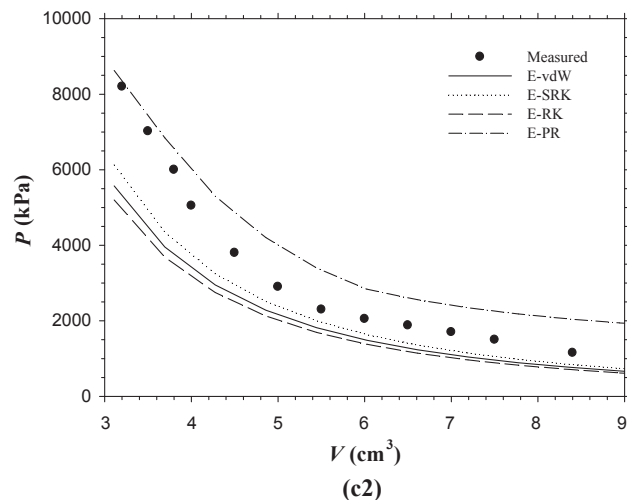
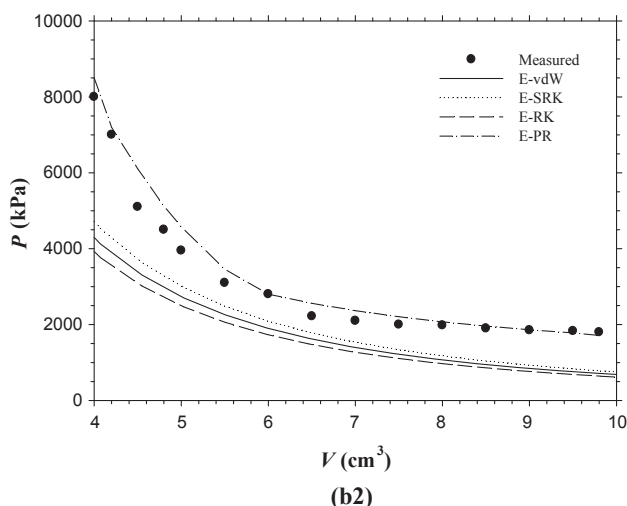
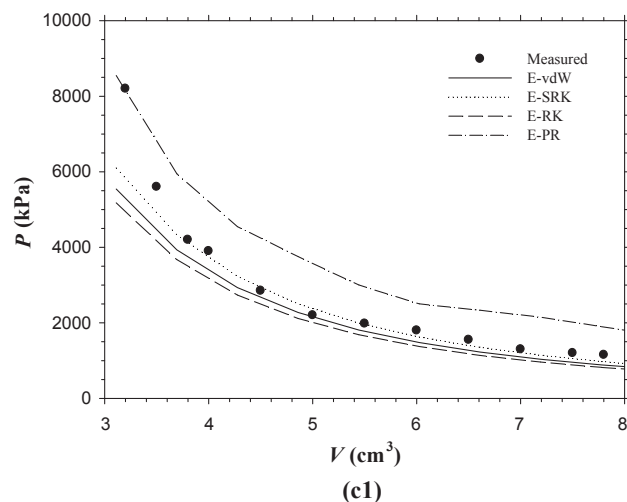
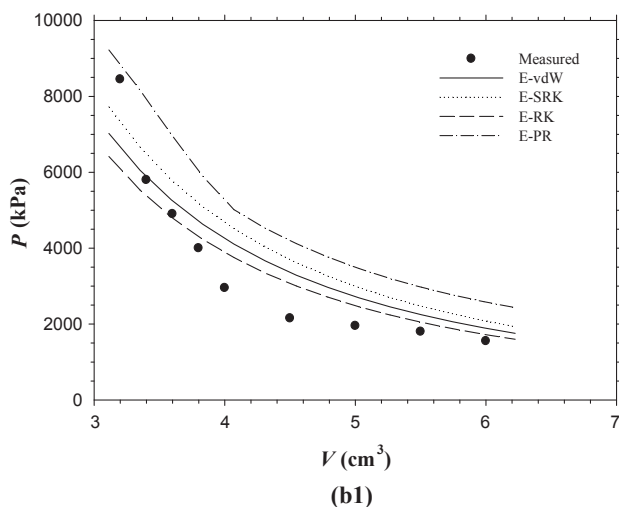


Fig. 3b. Measured [35] and calculated pressure–volume isotherms from the extended vdW, RK, SRK, and PR EOSs for the 90.00 mol.% $C_{10}H_{22}$ –10.00 mol.% CH_4 mixtures at $T = 325.15$ K and (b1) $r_p = 3.5$ nm and (b2) $r_p = 3.7$ nm.

Fig. 3c. Measured [35] and calculated pressure–volume isotherms from the extended vdW, RK, SRK, and PR EOSs for the 90.00 mol.% C_8H_{18} –10.00 mol.% CH_4 mixtures at $T = 311.15$ K and (c1) $r_p = 3.5$ nm and (c2) $r_p = 3.7$ nm.

mixtures are increased from 3390.6 to 3429.5 kPa and from 3115.1 to 3189.6 kPa by increasing the temperature from 299.15 to 324.15 K, while the measured bubble-point pressures at $r_p = 5.0$ nm are reduced at the same temperature elevations. The calculated P_b at $r_p = 5.0$ nm from the four extended EOSs share a similar value but opposite trend to the measured P_b , which increase with the increasing temperature. Compared to the measured P_b of the two N_2 – n - C_4H_{10} mixtures in nanopores at two different temperatures, the E-vdW, E-RK, E-SRK, and E-PR EOS are found to provide the calculated P_b with an overall percentage absolute deviation (AD%) of 2.16–8.21%, 7.40–14.86%, 0.50–8.47%, and 0.90–15.08%, respectively. It is seen from the table that the measured P_b for the 90.00 mol.% $C_{10}H_{22}$ –10.00 mol.% CH_4 mixture increase with the increasing temperature in the bulk phase and nanopores. Here, the calculated P_b in the nanopores from the four extended EOSs also increase at a higher temperature. The calculated P_b for the 90.00 mol.% C_8H_{18} –10.00 mol.% CH_4 mixture shares a similar pattern to that of the 90.00 mol.% $C_{10}H_{22}$ –10.00 mol.% CH_4 mixture. Thus, the four developed extended EOSs are capable to accurately predict the P_b of the confined mixtures in nanopores.

It should be noted from Table 1 that the measured P_b in the nanopores for the N_2 – n - C_4H_{10} mixture are reduced while the calculated P_b for the N_2 – n - C_4H_{10} and measured and calculated results for the $C_{10}H_{22}$ – CH_4 mixtures are increased with the increasing temperature. It should also be noted that the former mixture was measured based on the reservoir hydrocarbon-wetting shale core while the latter mixture was applied in

the SBA-15 and SBA-16. In the literature, the so-called selective sorption phenomenon, which means that different components in a mixture adsorbed onto the shale surface and absorbed into the organic matters to different extents, occurs when the mixture makes contact with the reservoir shale sample [40]. More specifically, the N_2 and n - C_4H_{10} are adsorbed/absorbed onto/into the shale sample at different sorption levels so that the actual compositions of the N_2 – n - C_4H_{10} mixture are different from the initial feed compositions. It was found that n - C_4H_{10} has a higher tendency to be sorbed onto the shale samples than N_2 [41]. Thus, the P_b in the nanopores of reservoir shale samples is mainly affected by the selective sorption of different components rather than the temperature change. In the proposed model, the following equations are added to consider the selective sorption for the N_2 – n - C_4H_{10} mixture case,

$$N_{np} = \frac{P_b V_{total}}{Z_{np} RT} \quad (30a)$$

$$N_{sor_N_2} = N_{inj} x_{inj_N_2} - N_{np} x_{np_N_2} \quad (30b)$$

$$N_{sor_C_4} = N_{inj} x_{inj_C_4} - N_{np} x_{np_C_4} \quad (30c)$$

On the other hand, the $C_{10}H_{22}$ and CH_4 share similar sorption amounts since they are normal alkanes [42]. Thus, the P_b of the $C_{10}H_{22}$ – CH_4 mixture are largely dependent on the temperature effect that they are increased at a higher temperature. In summary, for the four extended EOSs, the E-SRK EOS leads to the best calculation accuracy of P_b

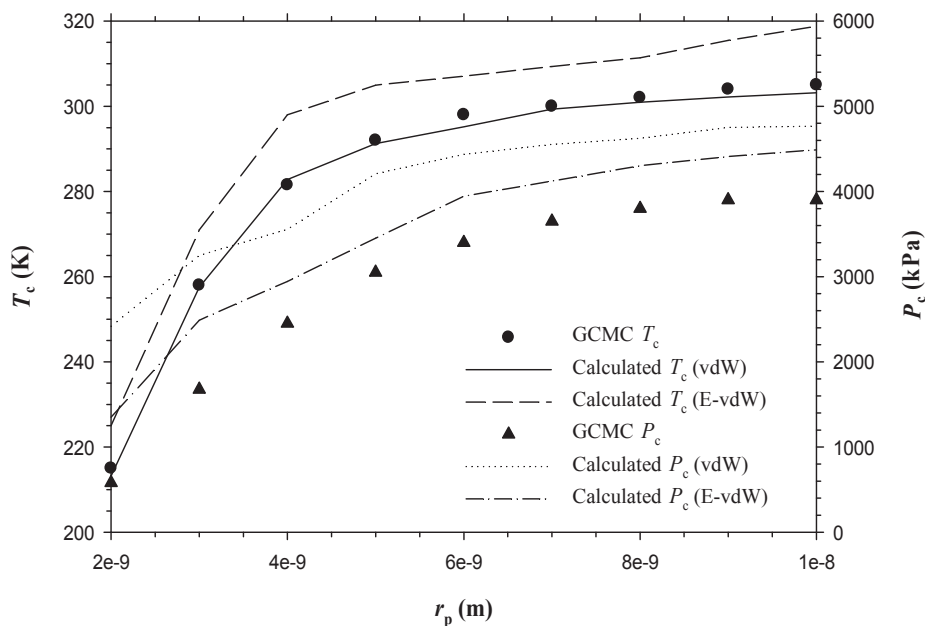


Fig. 4a. Calculated critical pressures and temperatures of C_2H_6 from the Grand Canonical Monte Carlo (GCMC) simulation [43] and from the vdW EOS including only molecule–molecule interaction and both the molecule–molecule and molecule–wall interactions in this study at $r_p = 2\text{--}10$ nm.

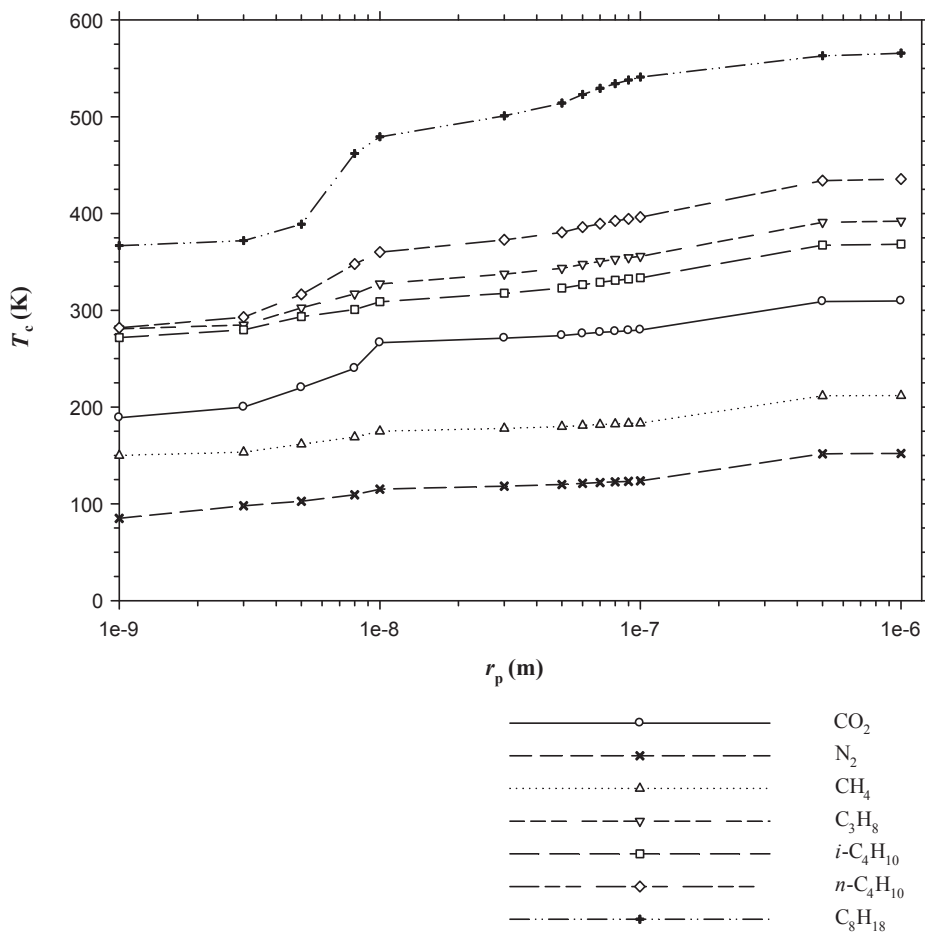


Fig. 4b. Calculated critical temperatures of CH_4 , C_3H_8 , i - and n - C_4H_{10} , C_8H_{18} , CO_2 , and N_2 from the vdW EOS including both the molecule–molecule and molecule–wall interactions at $r_p = 1\text{--}1,000$ nm.

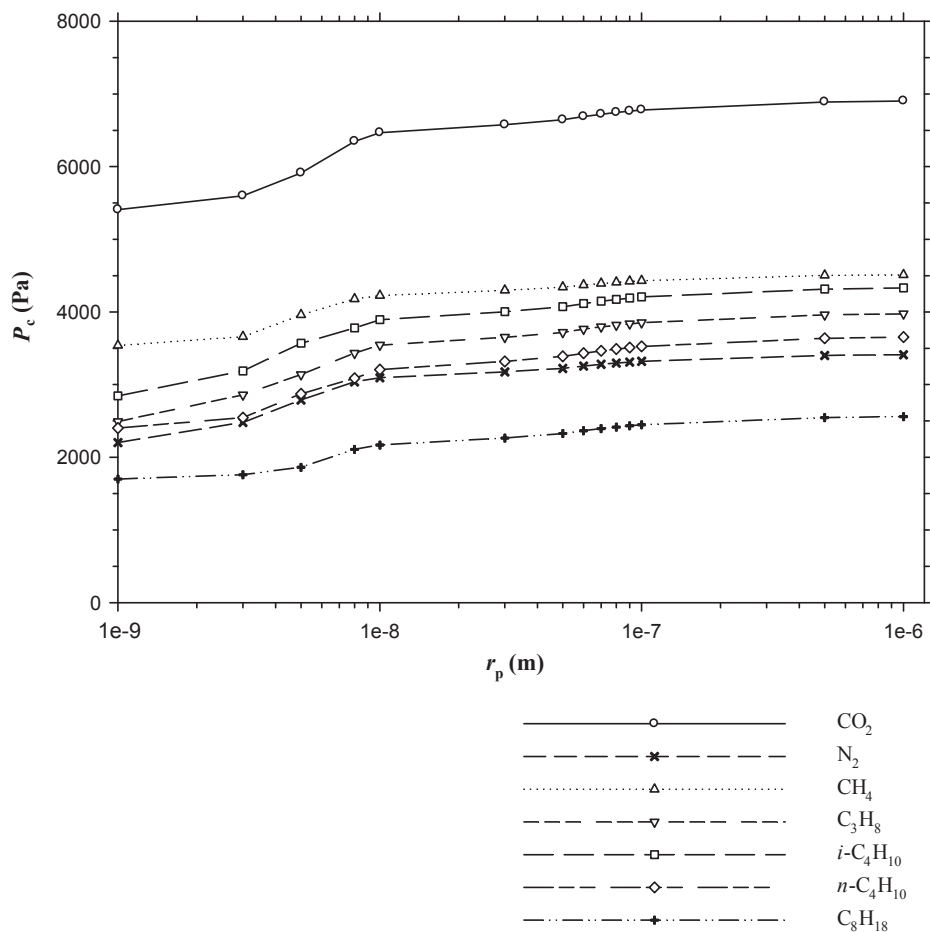


Fig. 4c. Calculated critical pressures of CH_4 , C_3H_8 , $i\text{-C}_4\text{H}_{10}$, $n\text{-C}_4\text{H}_{10}$, C_8H_{18} , CO_2 , and N_2 from the vdW EOS including both the molecule–molecule and molecule–wall interactions at $r_p = 1\text{--}1,000$ nm.

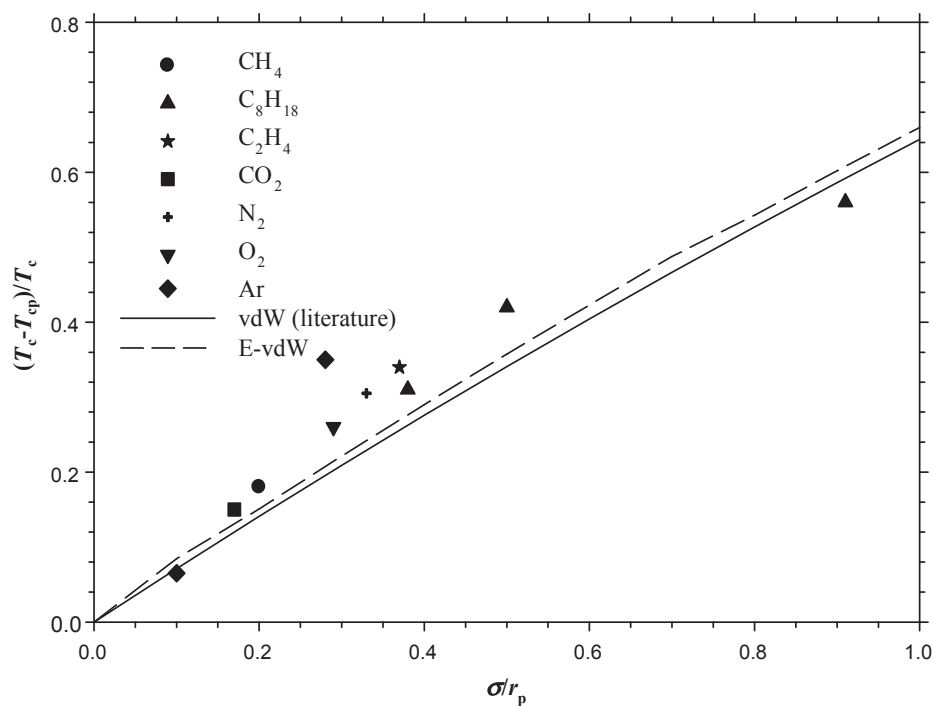


Fig. 5. Measured [46,47] and calculated shifts of the critical temperatures from the vdW EOS including only molecule–molecule interaction and both the molecule–molecule and molecule–wall interactions in this study with the variations of the pore radii.

with an overall average AD% (AAD%) of 9.37% and maximum absolute deviation (MAD%) of 27.00% for different systems at different pore radii and temperatures. Obviously, the E-PR may slightly overestimate P_b for the systems used in this study.

4.3. Critical properties

The critical pressures and temperatures of C_2H_6 at $r_p = 2$ –10 nm are calculated from the E-vdW EOS, which are compared to the calculated values from the Grand Canonical Monte Carlo (GCMC) simulation [43] and the vdW EOS only including the m-m interactions (referred to as the vdW EOS here for simplicity) and plotted in Fig. 4a. The calculated critical temperatures and pressures are found to reduce with the decreasing pore radius. The critical temperatures calculated from the vdW and E-vdW EOS in good agreement with the GCMC results, whereas the calculated critical pressures from the E-vdW EOS are more accurate than those from the vdW EOS. The small deviations between the calculated critical pressures and temperatures from the E-vdW EOS and GCMC are attributed to the incomplete consideration of the confinement phenomena in the proposed E-vdW EOS model. For example, no selective sorption phenomenon or capillary pressure is considered in the current model. However, it is still found that the E-vdW EOS outperforms the vdW EOS by concurrently modeling the m-m and m-w interactions.

In Figs. 4b and 4c, the critical pressures and temperatures of C_1 , C_3 , i - and n - C_4 , C_8 , CO_2 , and N_2 , at $r_p = 1$ –1000 nm are calculated, which are always decreased with the pore radius reductions. The critical temperature/pressure initiates to slightly decrease at $r_p = 500$ nm and remains until $r_p = 10$ nm, after which it decreases substantially by further reducing pore radius. Sudden slope changes occur, at $r_p = 5$ nm for C_8H_{18} and at $r_p = 3$ nm for the other components, after which the critical properties reduce more slowly with the pore radius. In consideration of the C_8H_{18} is 1 nm in molecular diameter [44] and the m-w interaction, several C_8 molecules are inferred to aggregate at $r_p > 5$ nm while only one or two C_8 molecules exist at $r_p \leq 5$ nm. For the other components, the critical pore radius is reduced to 3 nm since their molecular diameter is smaller than that of C_8H_{18} . Obviously, the pore radius exerts stronger effects on some aggregated molecules (intermolecularly) than a single molecule (intramolecularly). Moreover, it is found that a heavier alkane has a critical temperature but lower critical pressure. The critical temperatures of the alkanes, especially those with high-molecular weight like C_8H_{18} , are sensitive to the changes of pore radius when $r_p < 10$ nm [45]. It is worthwhile to mention that CO_2 is found to be a rather special case because its critical pressure and temperature are sensitive to the pore radius.

Fig. 5 shows the comparison of the measured shifts of critical temperatures for seven different components [46,47] with the solid points and the calculated values from the vdW EOS and E-vdW EOS with the respective solid and medium dash lines. The medium dashed line performs better than the solid line for the shifts of critical temperatures at different pore radii, which indicates that the E-vdW EOS including the m-m and m-w interactions performs better than the vdW EOS only including the m-m interactions. On a basis of the above-mentioned results, the proposed four extended EOSs have been validated to accurately predict the nanoscale phase behaviour and critical shifts. The currently-developed models, which should be noted, perform well but limited to calculate the IFTs of the pure and simple mixing systems. Moreover, some empirical parameters and numerical coefficients included in the models, more or less, may also introduce potential limitations for a general application.

5. Conclusions

Six major conclusions are obtained from this work as follows:

- An analytical generalized equation of state (EOS), which includes the confinement-induced pore radius effects and intermolecular interactions, is developed thermodynamically.
- Four new thermodynamic formulations, i.e., the extended van der

Waals (vdW), Redlich–Kwong (RK), Soave–Redlich–Kwong (SRK), and Peng–Robinson (PR) EOS, are proposed based on the new generalized EOS and applied to calculate the nanoconfined phase behaviour.

- The four extended cubic EOS are found to be able to predict the pressure–volume (P–V) diagrams of different systems in nanopores. More specifically, the E-RK may fail to accurately calculate the phase behaviour at high temperatures. Furthermore, the E-PR EOS is more accurate for the liquid phase calculations.
- The calculated P–V diagrams for the pure component in nanopores from the extended EOS shift toward the upper right in comparison with the bulk phase case and the EOS only including the m-m interactions. The negative pressure state, which is always treated as physically meaningless for gases, is completely avoided by adding the m-w interaction into the extended EOS models.
- The E-vdW, E-RK, and E-SRK EOS are found to accurately calculate the bubble-point pressures (P_b) of different confined pure and mixing fluids at different temperatures in nanopores. In comparison with the measured P_b for the four different confined mixing fluids in nanopores, the three extended EOSs provide accurate values of P_b with overall percentage average absolute deviations (AAD%) of 10.95%, 12.07%, and 9.37%, respectively. The E-PR is found to overestimate P_b for the systems used in this study.
- The critical pressure and temperature shift under strong confinement effects in the nanopores. The proposed extended EOS are capable to accurately predict the critical properties and their shifts. Moreover, the critical pressure and temperature are not monotonically reduced with the decreasing pore radius, a bottom limit of which can be determined by using the proposed extended EOS, which is, for example, 5 nm for C_8H_{18} .

Acknowledgements

The authors would like to acknowledge the Petroleum Systems Engineering at the University of Regina. They also want to acknowledge the financial supports from Petroleum Technology Research Centre (PTRC) and Mitacs Canada.

Appendix A. Supplementary data

Supplementary data to this article can be found online at <https://doi.org/10.1016/j.fuel.2019.03.095>.

References

- [1] Takbiri-Borujeni A, Fathi E, Kazemi M, Belyadi F. An integrated multiscale model for gas storage and transport in shale reservoirs. *Fuel* 2019;237:1228–43.
- [2] Anwar A, Garforth A. Challenges and opportunities of enhancing cold flow properties of biodiesel via heterogeneous catalysis. *Fuel* 2016;173:189–208.
- [3] Hao P, Shi Y, Li S, Zhu X, Cai N. Correlations between adsorbent characteristics and the performance of pressure swing adsorption separation process. *Fuel* 2018;230:9–17.
- [4] Wang L, Yu W. Mechanistic simulation study of gas Puff and Huff process for Bakken tight oil fractured reservoir. *Fuel* 2019;239:1179–93.
- [5] Zhang K, Jia N, Liu L. CO_2 storage in fractured nanopores underground: Phase behaviour study. *Appl Energy* 2019;238:911–28.
- [6] Singh JK, Docherty H, Cummings PT. Phase transition under confinement. *Comput Nanosci R Soc Chem* 2011:82–108.
- [7] Marti A, Hähner G, Spencer ND. Sensitivity of frictional forces to pH on a nanometer scale: a lateral force microscopy study. *Langmuir* 1995;11:4632–5.
- [8] Zhang K, Jia N, Liu L. Adsorption thicknesses of confined pure and mixing fluids in nanopores. *Langmuir* 2018;34:12815–26.
- [9] Czarnota R, Janiga D, Stopa J, Wojnarowski P. Acoustic investigation of CO_2 mass transfer into oil phase for vapor extraction process under reservoir conditions. *Int J Heat Mass Transf* 2018;127:430–7.
- [10] Wojnarowski P, Czarnota R, Janiga D, Stopa J. Novel liquid-gas corrected permeability correlation for dolomite formation. *Int J Rock Mech Min Sci* 2018;112:11–5.
- [11] Lifton VA. Microfluidics: an enabling screening technology for enhanced oil recovery (EOR). *Lab Chip* 2016;16:1777–96.
- [12] Zhang K, Jia N. Confined fluid interfacial tension calculations and evaluations in nanopores. *Fuel* 2019;237:1161–76.
- [13] Awadalla T, Voskov D. Modeling of gas flow in confined formations at different scales. *Fuel* 2018;234:1354–66.

- [14] Coasne B, Galarneau A, Pellenq RJM, Di Renzo F. Adsorption, intrusion and freezing in porous silica: the view from the nanoscale. *Chem Soc Rev* 2013;42:4141–71.
- [15] Yang Q, Jin B, Banerjee D, Nasrabadi H. Direct visualization and molecular simulation of dewpoint pressure of a confined fluid in sub-10 nm slit pores. *Fuel* 2019;235:1216–23.
- [16] Bakhshian S, Hosseini SA. Prediction of CO₂ adsorption-induced deformation in shale nanopores. *Fuel* 2019;241:767–76.
- [17] Xu C, You Z, Kang Y, You L. Stochastic modelling of particulate suspension transport for formation damage prediction in fractured tight reservoir. *Fuel* 2018;221:476–90.
- [18] Bajaj S, Haverty MG, Arróyave R, Shankar S. Phase stability in nanoscale material systems: extension from bulk phase diagrams. *Nanoscale* 2015;7:9868–77.
- [19] Digilov R. Kelvin equation for menisci of nanosize dimensions. *Langmuir* 2000;16:1424–7.
- [20] Emery VJ, Kivelson SA. Importance of phase fluctuations in superconductors with small superfluid density. *Nature* 1995;374:434–7.
- [21] Harris JG, Yung KH. Carbon dioxide's liquid-vapor coexistence curve and critical properties as predicted by a simple molecular model. *J Phys Chem* 1995;99:12021–4.
- [22] Liu L, Huang CZ, Huang G, Baetz B, Pittendrigh SM. How a carbon tax will affect an emission-intensive economy: a case study of the Province of Saskatchewan, Canada. *Energy* 2018;159:817–26.
- [23] Zhang K, Gu Y. Two different technical criteria for determining the minimum miscibility pressures (MMPs) from the slim-tube and coreflood tests. *Fuel* 2015;161:146–56.
- [24] Molla S, Mostowfi F. Microfluidic PVT-saturation pressure and phase-volume measurement of black oils. *SPE Reserv Eval Eng* 2017;20:233–9.
- [25] Zhang K, Jia N, Li S, Liu L. Millimeter to nanometer-scale tight oil–CO₂ solubility parameter and minimum miscibility pressure calculations. *Fuel* 2018;220:645–53.
- [26] Teklu TW, Alharthy N, Kazemi H, Yin X, Graves RM, AlSumaiti AM. Phase behavior and minimum miscibility pressure in nanopores. *SPE Reserv Eval Eng* 2014;17:396–403.
- [27] Okamoto H, Massalski TB. Guidelines for binary phase diagram assessment. *J Phase Equilibria* 1993;14:316–35.
- [28] Zarragoicoechea GJ, Kuz VA. Critical shift of a confined fluid in a nanopore. *Fluid Phase Equilib* 2004;220:7–9.
- [29] Zhang K, Jia N, Zeng F, Luo P. A new diminishing interface method for determining the minimum miscibility pressures of light Oil–CO₂ systems in bulk phase and nanopores. *Energy Fuels* 2017;31:12021–34.
- [30] Whitson CH, Brule MR. Phase Behavior. Richardson, Texas: Monogr Ser SPE; 2000.
- [31] Yu Y-X, Gao G-H. Lennard-Jones chain model for self-diffusion of n-alkanes. *Int J Thermophys* 2000;21:57–70.
- [32] Sharma RV, Sharma KC. The structure factor and the transport properties of dense fluids having molecules with square well potential, a possible generalization. *Phys A Stat Mech Its Appl* 1977;89:213–8.
- [33] Zhang K, Jia N, Li S, Liu L. Quantification and Evaluation of Thermodynamic Miscibility in Nanoconfined Space. *Ind Eng Chem Res* 2019;58:4609–24.
- [34] Liu Y, Li HA, Tian Y, Jin Z, Deng H. Determination of the absolute adsorption/desorption isotherms of CH₄ and n-C₄H₁₀ on shale from a nano-scale perspective. *Fuel* 2018;218:67–77.
- [35] Cho H, Bartl MH, Deo M. Bubble point measurements of hydrocarbon mixtures in mesoporous media. *Energy Fuels* 2017;31:3436–44.
- [36] Sandler SI. The generalized van der Waals partition function. I. Basic theory. *Fluid Phase Equilib* 1985;19:238–57.
- [37] Lommerse JPM, Stone AJ, Taylor R, Allen FH. The nature and geometry of intermolecular interactions between halogens and oxygen or nitrogen. *J Am Chem Soc* 1996;118:3108–16.
- [38] Liu L, Huang G, Baetz B, Huang CZ, Zhang K. A factorial ecologically-extended input-output model for analyzing urban GHG emissions metabolism system. *J Clean Prod* 2018;200:922–33.
- [39] Imre AR. How to generate and measure negative pressure in liquids? *Soft matter under Exog. impacts*. Springer; 2007. p. 379–88.
- [40] Clarkson CR, Haghsheenas B. Modeling of supercritical fluid adsorption on organic-rich shales and coal. *SPE Unconv. Resour. Conf. : Society of Petroleum Engineers*; 2013.
- [41] Xiong F, Wang X, Amooie MA, Soltanian MR, Jiang Z, Moortgat J. The shale gas sorption capacity of transitional shales in the Ordos Basin, NW China. *Fuel* 2017;208:236–46.
- [42] Falk K, Pellenq R, Ulm FJ, Coasne B. Effect of chain length and pore accessibility on alkane adsorption in kerogen. *Energy Fuels* 2015;29:7889–96.
- [43] Pitakbunkate T, Balbuena PB, Moridis GJ, Blasingame TA. Effect of confinement on pressure/volume/temperature properties of hydrocarbons in shale reservoirs. *SPE J* 2016;21:621–34.
- [44] Zhang K, Gu Y. Two new quantitative technical criteria for determining the minimum miscibility pressures (MMPs) from the vanishing interfacial tension (VIT) technique. *Fuel* 2016;184:136–44.
- [45] Zhang K, Jia N, Li S, Liu L. Thermodynamic phase behaviour and miscibility of confined fluids in nanopores. *Chem Eng J* 2018;351:1115–28.
- [46] Zarragoicoechea GJ, Kuz VA. van der Waals equation of state for a fluid in a nanopore. *Phys Rev E* 2002;65:21110.
- [47] Islam AW, Patzek TW, Sun AY. Thermodynamics phase changes of nanopore fluids. *J Nat Gas Sci Eng* 2015;25:134–9.